iJET EXPLORE International Journal of Engineering & Technology
CENTRE OF PROFESSIONAL RESEARCH PUBLICATIONS
ISSN 2049-3444

International Journal of Engineering and Technology Volume 2 No. 4, April, 2012

Three-Dimensional Thermal Finite Element Modeling for Keyhole Plasma Arc Welding of 2205 Duplex Stainless Steel Plates

M. A. Daha[1], G. A. Nassef[1], I. A. Abdallah[1], and H. M. AbouSeeda[2]
[1]Production Engineering Department, Faculty of Engineering, Alexandria University, Alexandria, Egypt
[2]Structural Engineering Department, Faculty of Engineering, Alexandria University, Alexandria, Egypt

ABSTRACT

A three-dimensional thermal transient finite element model has been developed to estimate the weld geometry and to analyze the temperature field due to the keyhole plasma arc welding (PAW) in 2205 duplex stainless steel. An adaptive heat source model is proposed for the numerical analysis of the process, considering the "bugle-like" configuration feature of keyhole PAW welds. The thermal analysis has revealed temperature contours that indicate the size and geometry of the weld fusion zone (FZ). The initial models are validated against experimental data and show very good correlation. Such good correlation indicates the validity of the numerical heat transfer model and the analytical fluid flow model. A variety of welding heat inputs are then simulated. Effect of welding heat input on the size and geometry of the weld fusion zone are established.

Keywords: *keyhole plasma arc welding, duplex stainless steel, finite element analysis, adaptive heat source model, weld geometry, temperature field*

1. INTRODUCTION

Duplex stainless steels (DSSs) represent a class of stainless steels with dual microstructure consisting of approximately equal proportions of ferrite and austenite phases. This balanced microstructure offers a favorable combination of mechanical strength and corrosion resistance. The volume fractions of ferrite and austenite in welded DSSs depends upon the thermal history. Owing to their superior mechanical properties and corrosion characteristics, DSSs have been employed as structural materials in various industrial sectors, such as offshore construction, chemical, petrochemical, pulp and paper, power generation, desalination, and oil and gas. Recently, in view of increasing applications of DSSs, it is important to have a better understanding of the issues associated with welding of DSSs.

During conventional fusion welding processes of DSSs joints, the material is subjected to very high heating and cooling rates, that has unfavorable significant influence on the weld quality. For this reason, plasma arc welding of DSSs joints finds increasing demand due to the lower cooling rates and with the advantages of high welding speed providing higher productivity. The most commonly used technique of PAW is the keyhole mode. The high energy density of keyhole PAW causes a temperature rise above the material melting point. In fact, the temperature reaches the boiling point and converts the melt metal to a superheated vapor. The intense evaporation of the metal often results in the formation of a deep and narrow vapor cavity within the molten weld pool known as the "keyhole" (Figure 1).

The keyhole PAW offers significant advantages over conventional tungsten inert gas (TIG) welding in terms of penetration depth, joint preparation and thermal distortion. In addition, the keyhole PAW can be used for butt welds from approximately 3 mm up to 7-8 mm thick with a single pass; by comparison, the TIG method is only suitable for butt welds up to approximately 3-4mm thick [1]. These are some of the reasons justifying the substitution of TIG welding with plasma keyhole welding. The temperature profile around the keyhole and the weld pool has a great influence on the formation and stability of the keyhole. Therefore, it is of great significance to model and simulate the temperature distribution and weld pool geometry in the keyhole PAW process.

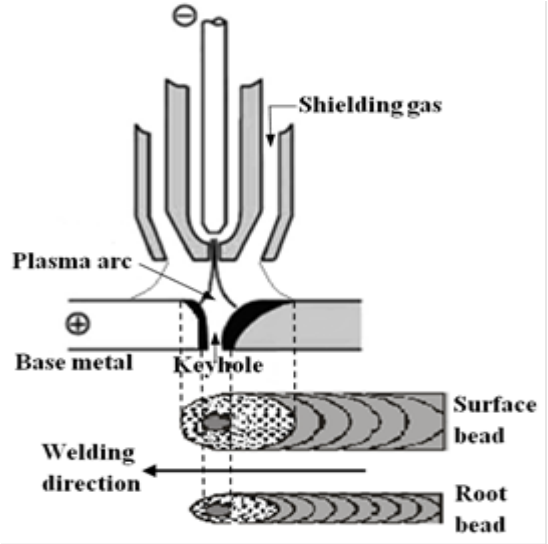

Figure 1: Keyhole Plasma Arc Welding Technique

2. STATE OF THE ART

In recent years, plasma welding of duplex stainless steels has become of great interest in the industry; however, the research woks in this field are relatively limited. Urena *et al*. [2] have determined the optimum welding conditions, in terms of heat input, microstructure, and hardness, for plasma welding of 2205 duplex stainless steel that is 3 mm thick. Zheng *et al*. [3] have investigated the effects of a dual-torch technique using plasma welding followed by TIG welding on the microstructure and corrosion properties of 2205 DSS. Taban [4] investigated the effects of plasma welding and of combined plasma and TIG welding on the microstructure and toughness of SAF 2205 DSS. In further work, Taban [5] investigated the effect of plasma welding on the toughness of UNS 32750 super duplex stainless steel. Migiakis *et al*. [6] focused on plasma keyhole welding of UNS S32760 (Zeron 100) super duplex stainless steel and studied the microstructure, tensile strength, and impact toughness of the weldments.

Keanini and Rubinsky [7] employed 3D finite element-based simulation of the plasma arc welding process to study the effect of the plate ambient temperature on the weld pool's three-dimensional capillary surface shape and temperature fields. Fan and Kovacevic [8] developed a mathematical model to describe the heat transfer and fluid flow in stationary keyhole plasma arc welding. Wu *et al*. [9] developed a three-dimensional finite element model for keyhole plasma arc welding and concluded that a modified three-dimensional conical heat source model is an appropriate model to reflect the nonlinear decay of the heat intensity distribution along the direction of the workpiece thickness. In another paper, Wu *et al*. [10] employed an adaptive heat source model for keyhole PAW that combined a double-ellipsoidal volumetric heat source and a cylindrical volumetric heat source. Wang *et al*. [11] simulated the keyhole PAW through a 3D FE model and investigated the effects of workpiece thicknesses on the moments of keyhole formation, and stable keyholes have been analyzed. In this paper, dynamic evolution of geometrical shape, the dimensions and fluid flow of the molten pool and the keyhole have been simulated via the three-dimensional thermal keyhole PAW finite element model based on the adaptive heat source model proposed by Wu *et al*. [10]. In addition, the developed thermal model has been experimentally verified by comparing the predicted weld pool geometry and size obtained from the thermal analysis with the experimental results.

3. FINITE ELEMENT ANALYSIS

In this investigation, the heat transfer and the fluid flow during keyhole PAW of a 2205 DSS plate was simulated using a full three-dimensional thermal finite element formulation that was implemented in ABAQUS® code [12]. The model was applied to evaluate the temperature field and the weld pool geometry and size for various keyhole PAW conditions. For the accuracy of the calculations, verification of the model was performed through comparing the predicted results with metallographic weld cross-section data. The simulated welding parameters are given in Table 1.

Table 1: Welding Parameters for a 6.8 mm Thick 2205 DSS Plates

	Weld 1	Weld 2	Weld 3
Welding current (A)	140	140	140
Arc Voltage (V)	28	28	28
Welding Speed (mm/min)	105	120	135
Arc efficiency	0.5	0.5	0.5
Nominal heat input (kJ/mm)	2.25	1.96	1.75
Ambient temperature (K)	294	294	294

3.1 Model Geometry and Meshing

Finite element thermal simulation of the keyhole PAW process has been performed on a DSS plate butt joint; the size of the plate is 160 mm × 160 mm and the thickness is

6.8 mm. The butt-welded plate was symmetrical about the plane passing through the weld centerline. The geometrical model was partitioned into various regions; each region consisted of meshes of different densities. Fine meshes were chosen in the welding region to apply the heat flux more accurately when the moving heat source passes the region at specific time steps, where the temperature gradients are expected to be the most severe. Conversely, regions away from the weld are meshed with a coarse mesh. Between the refined and the far-field regions, transition regions were used. Figure 2 shows the 3D symmetrical graded mesh of the welded plate. The full symmetrical plate model has 195840 eight-node linear hexahedral elements and 221531 nodes. Eight-node 3D hexahedral elements of the ABAQUS® type DC3D8 were used in the heat transfer analysis.

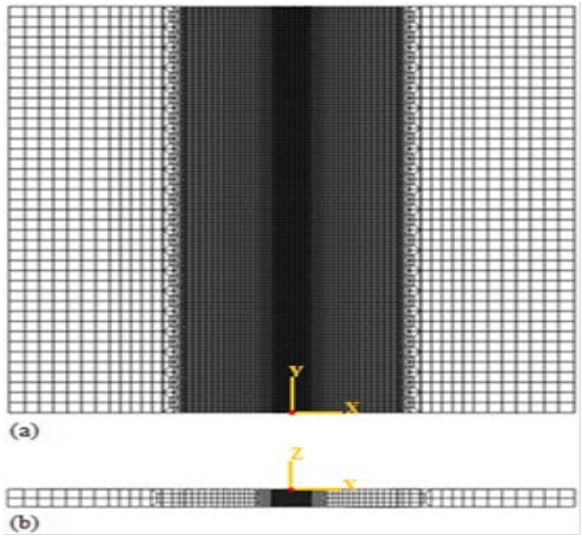

Figure 2: 3D Symmetrical Graded Finite Element Mesh: (a) Top view; (b) Side view

3.2 Material Properties

The finite element transient thermal analysis requires accurate values of the thermal conductivity and the specific heat up to the melting point. Temperature-dependent thermo physical properties of the 2205 DSS base material used in this study, i.e., the thermal conductivity and specific heat, are plotted in Figure 3. Other properties used in the analysis are summarized in Table 2. The chemical composition of the base material is given in Table 3.

Table 2: Material properties for 2205 DSS used in the calculations

Property	Value
Latent heat of fusion (kJ/kg)	500
Liquidus Temperature (K)	1773
Solidus temperature (K)	1658
Density of metal (kg/m^3)	7860
Surface emissivity	0.7

Table 3: Chemical Composition of the Base Metal (in wt%)

C	Si	Mn	P	Cr	Cu	Ni	Mo	Ti	V	Al	Nb	Fe	Co
0.012	0.46	1.48	0.037	22.55	0.12	5.64	3.13	0.013	0.064	0.06	0.04	66.35	0.04

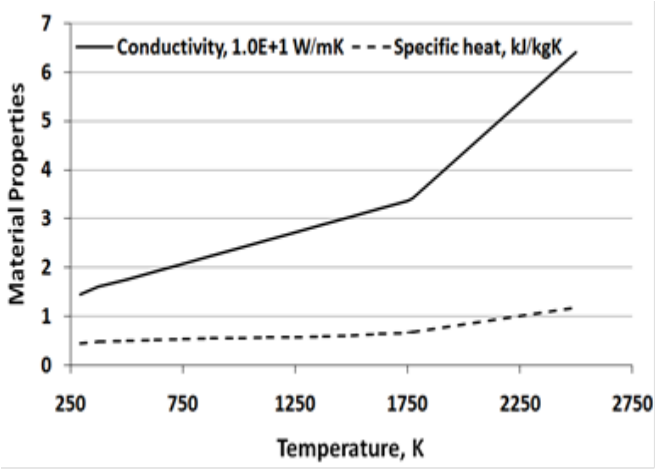

Figure 3: Thermo Physical Material Properties for 2205 DSS

3.3 Thermal analysis

3.3.1 Governing equations

In transient heat transfer theory, the spatial and temporal temperature $T(x, y, z, t)$ of the weld plate satisfies the following transient non-linear heat transfer governing differential equation:

$$\frac{\partial}{\partial x}\left(k_x \frac{\partial T}{\partial x}\right)+\frac{\partial}{\partial y}\left(k_y \frac{\partial T}{\partial y}\right)+\frac{\partial}{\partial z}\left(k_z \frac{\partial T}{\partial z}\right)+q=\rho c\left(\frac{\partial T}{\partial t}\right) \tag{3.1}$$

Here, k_x, k_y and k_z are the thermal conductivities in the x, y, and z directions, respectively; ρ is the density; c is the specific heat of the material; and q is the internal heat source rate.

To solve the above differential equation, initial and boundary conditions must be specified. If T_0 is the atmospheric temperature or room temperature, the initial condition is:

$$T(x, y, z, 0)=T_0(x, y, z) \tag{3.2}$$

3.3.2 Boundary Conditions

To consider heat losses, both the thermal radiation and convection from the outer surface are assumed and defined by:

$$k_n \frac{\partial T}{\partial n}-q+h(T-T_0)+\sigma\varepsilon\left(T^4-T_0{}^4\right)=0 \tag{3.3}$$

where k_n is the thermal conductivity normal to the surface, σ is the Stefan Boltzmann constant (5.67×10^{-8} W m^{-2} K^{-4}). Radiation losses are dominant for higher temperatures in and around the weld zone, where it becomes the primary mechanism of heat dissipation. Away from the weld zone at lower temperatures, convection plays a vital role in heat losses. Therefore, all free surfaces heat losses are applied and calculated by Vinokurov's empirical relationship [18, 13 and 14], which combines the effect of both convection and radiation as:

$$h=2.41\times10^{-3}\varepsilon T^{1.61} \tag{3.4}$$

where h is the combined heat transfer coefficient, ε is the emissivity or the degree of blackness of the surface of the body, and T is the temperature in K.

The effect of the fluid flow has significant effects on the temperature distribution and on the shape of the weld pool. To account for the heat transfer due to fluid flow, an artificial increase in the thermal conductivity above the melting temperature is used [15-20]. In this study, it was assumed that the value of the thermal conductivity is approximately three times as large as that at room temperature when the temperature is higher than the melting point. The thermal effects due to solidification of the weld pool are modeled by taking into account the latent heat for fusion. The latent heat is considered between the solidus temperature and the liquidus temperature.

3.3.2 Heat Source Model

A variety of heat source models can be used to simulate the heat input from the welding torch, e.g., triangular, conical, double-ellipsoidal, and adaptive heat sources. The choice of heat source model depends upon the type of welding process. In this study, for keyhole PAW, the heat from the moving welding arc is modeled by an adaptive heat source presented by Wu et al. [10] to match the weld pool configuration feature of keyhole PAW welds. The adaptive heat source model combines a double-ellipsoidal volumetric heat source acts at the upper part of the workpiece and a cylindrical volumetric heat source exerts at the lower part of the workpiece. The net heat input q to the workpiece from the keyhole PAW arc is described as follows:

$$q=\eta IV \tag{3.5}$$

where η is the arc efficiency, I is the electric current, and V is the voltage. The power of the combined heat source, q_{dv} and q_{cv}, describing the power inside the double-

ellipsoidal volumetric heat source and the cylindrical volumetric heat source, can be expressed as:

$$q_{dv} = \beta_1 q \tag{3.6}$$

$$q_{cv} = \beta_2 q \tag{3.7}$$

$$q = q_{dv} + q_{cv} = (\beta_1 + \beta_2) q \tag{3.8}$$

where β_1 and β_2 are the power distribution factors which give the fraction of heat deposited in the upper and lower parts of the workpiece, respectively.

If $z < c$, $y < 0$,

$$Q_V(x,y,z) = \frac{12\sqrt{3}\beta_1 q}{\pi\sqrt{\pi} a b_1 c} \frac{b_1}{(b_1 + b_2)} \exp\left(-\frac{3x^2}{a^2} - \frac{3y^2}{b_1^2} - \frac{3z^2}{c^2}\right) \tag{3.9}$$

If $z < c$, $y \geq 0$,

$$Q_V(x,y,z) = \frac{12\sqrt{3}\beta_1 q}{\pi\sqrt{\pi} a b_2 c} \frac{b_2}{(b_1 + b_2)} \exp\left(-\frac{3x^2}{a^2} - \frac{3y^2}{b_2^2} - \frac{3z^2}{c^2}\right) \tag{3.10}$$

If $z \geq c$,

$$Q_V(r,z) = \frac{6\beta_2 q}{\pi r_1 H(mH + 2r_1)} \exp\left(-\frac{3r^2}{r_1^2}\right)\left[1 + \frac{m(z-c)}{r_1}\right] \tag{3.11}$$

where a, b_1, b_2, and c are the characteristics parameters of the double ellipsoidal volumetric heat source, $m = r_1/H$, r_1 is the radius of the cylindrical region, and H is the height of the cylindrical heat source. $r^2 = x^2 + y^2$, $H = L - c$, and L is the workpiece thickness. The parameters β_1, β_2, a, b_1, b_2, c, and r_1 of the heat source can be adjusted to create a desired melted zone.

Using equations (3.9, 3.10, and 3.11), a user subroutine DFLUX has been written in FORTRAN to define the non-uniform distributed flux as a function of time, position, and temperature during the heat transfer analysis. The user subroutine DFLUX has been embedded into ABAQUS/Standard to automatically detect the position of the welding pool and to calculate the volumetric heat flux, then to assign it to the correct elements of the welding plates while the torch is moving through.

4. VERIFICATION OF THE FINITE ELEMENT MODEL

To confirm the accuracy of the thermal finite element analysis method used in the present investigation, a single-pass keyhole PAW experiments were conducted on a 2205 DSS workpiece with a thickness of 6.8 mm. Straight plate edges perpendicular to the plate surface have been prepared. The welding parameters chosen for the experiments were as follows: V = 28 Volts, I = 140 A, η = 0.50 and a welding speed = 0.002 mm/sec. PAW in keyhole mode was accomplished without any filler metal and by using direct current electrode negative (DCEN) polarity. The results obtained from the thermal analysis were compared with the experimental results. Figure 4 shows the typical weld fusion zone shape and size obtained from the experiments and the corresponding weld fusion zone shape and size obtained from the simulation model. It can be observed that the predicted weld fusion zone geometry and width at both top and bottom surfaces show good agreement with those measured experimentally.

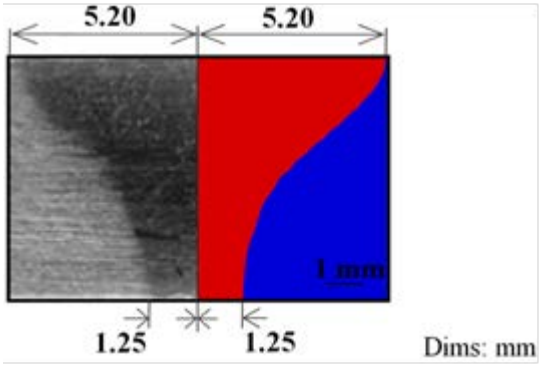

Figure 4: Comparison of the Weld Fusion Zone: Experiment vs. Simulation

5. RESULTS AND DISCUSSION

Figure 5 shows the temperature distribution of the 6.8 mm thick plate when the keyhole PAW torch passes through the whole plate in the (y-direction). It is noticed that all of the material with in the fusion zone rises in temperature above the melting point, reaching 3623 *K* for a heat input of 1.96 kJ/mm . This high temperature is the main attribute in the formation of the keyhole, converting liquid to vapor. Figure 6 shows isotherms on the lateral (xz-plane) at different instants of time. These curves indicate the pattern of heat flow in the weldment. These curves are drawn for V = 28 Volts, I = 140 A, η = 0.50 and a welding speed = 0.002 mm/sec. A study of the isotherm sequence in Figure 6 provides the theory about the nature of heat

flow in the keyhole plasma weldment. To observe the molten-zone growth, the isotherm corresponding to the liquidus temperature (1773 *K*) is plotted and examined. The isotherm corresponding to 1773 *K* will show how fast the fusion zone is growing. Heat input to the welding pool is transferred quickly, first in the thickness direction and then in the width direction to reach a uniform distribution. The isotherms at time ($t = t_o + 0.60$ S) indicating that the fusion zone ($T = 1773$ *K*) has the shape of a reversed bugle. The fusion zone is completely formed at ($t = t_o + 1.15$ S), the half fusion zone width is 5.20 mm on the top surface and 1.25 mm on the bottom surface for a heat input of 1.96 kJ/mm. Thus, the numerical results are in good agreement with the experimental measurements.

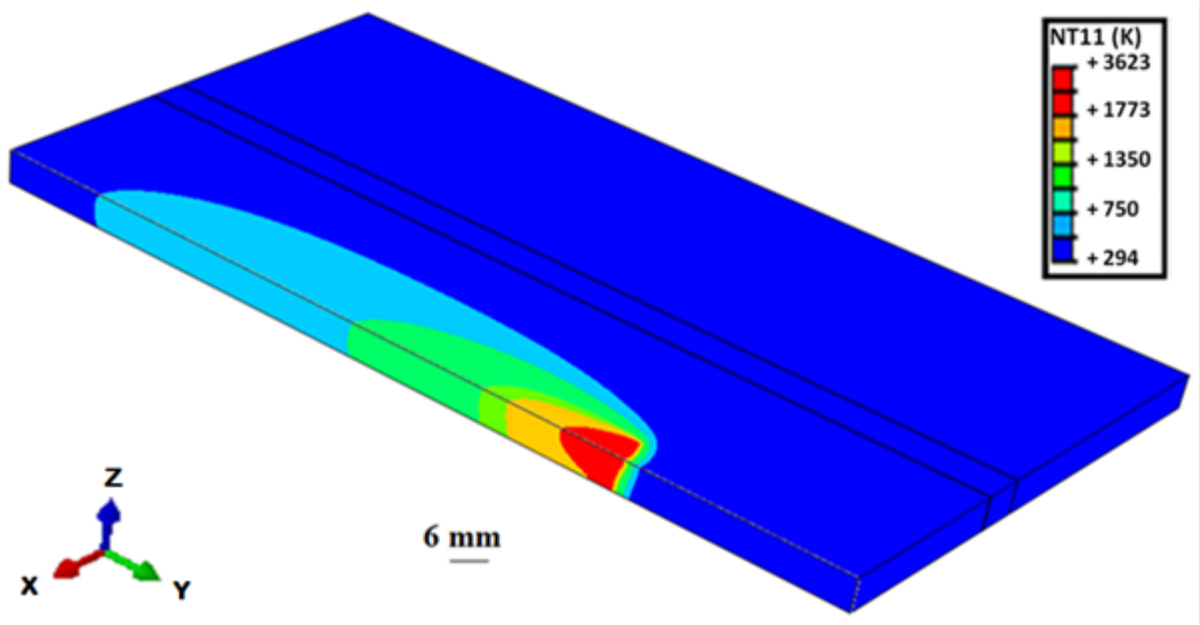

Figure 5: Three-Dimensional Temperature Distribution in the 6.8 mm Thick Plate

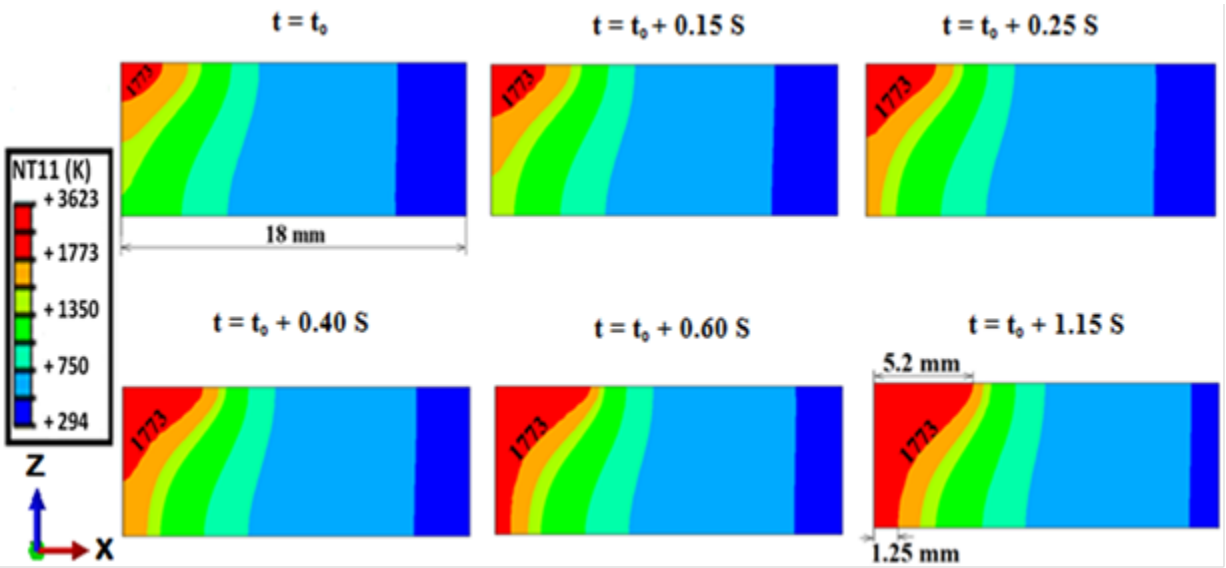

Figure 6: Isotherms in the Lateral Plane

Effect of heat input can be easily studied using the thermal finite element model. Figure 7 shows the isotherms on the top surface for different heat input values. The inner isotherm, representative of the liquidus temperature, demonstrates the geometrical characteristics of the weld pool. In this study, different values of heat input were obtained by changing the welding speed. It can be noted that the heat input has a minor effect on the temperature distribution on the top surface of the welded plates. Figure 8 shows clearly the three shapes of the weld pool profiles for three different heat input. The solid lines show the predicted weld pool boundary as defined by the liquidus temperature. In terms of the weld fusion zone geometry and size, increasing the heat input provides a wider weld bead and more fusion of materials in the lateral direction. It is also observed that when the heat input is increased, more welding energy is concentrated towards the upper part of the plate compared with the lower part. The predicted weld pool shapes, however, show only a gradual change in weld pool cross-sectional width with depth. Therefore, using such finite element model, it is possible to investigate the weld fusion zone size and geometry under any requested welding parameters.

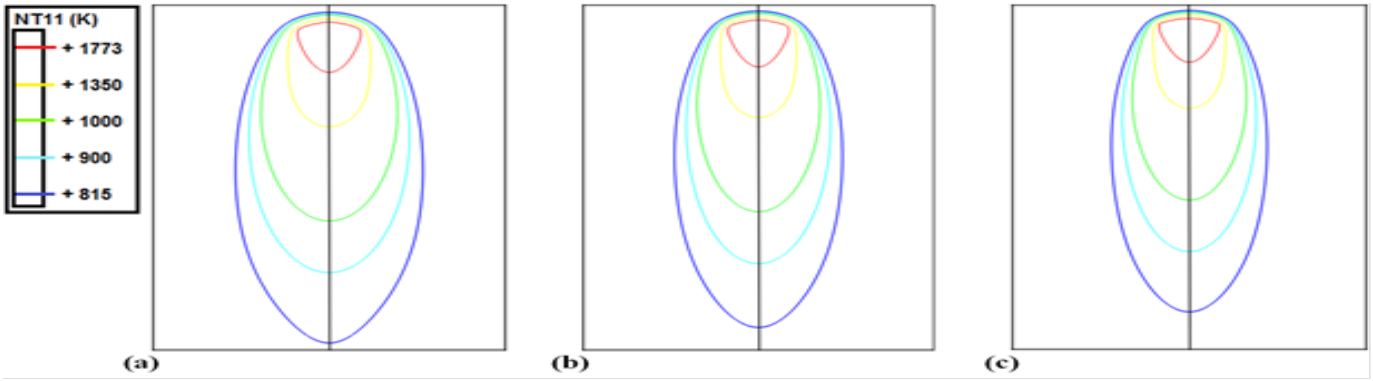

Figure 7: Isotherms on the Top Surface for a Heat Input of (a) 2.25 kJ/mm, (b) 1.96 kJ/mm, and (c) 1.75 kJ/mm

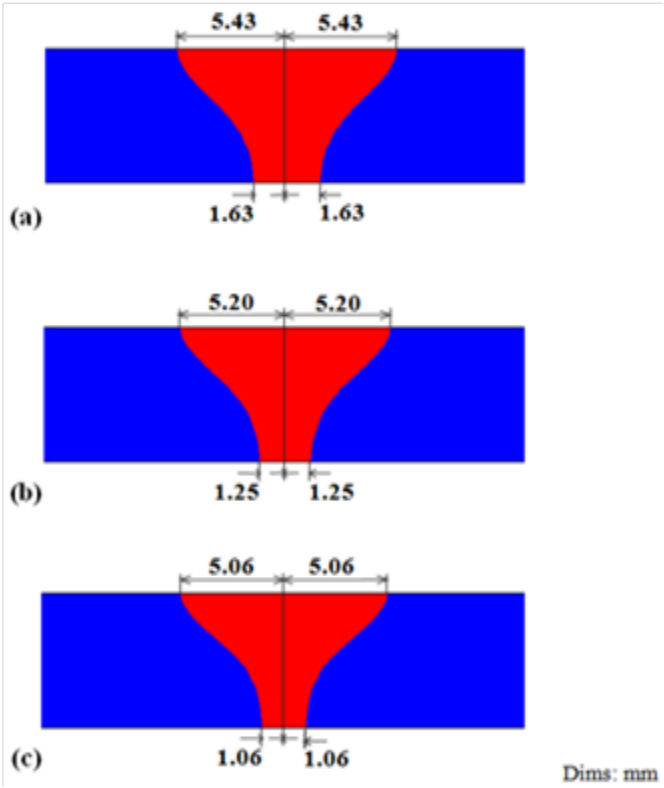

Figure 8: Weld Fusion Zone for a Heat Input of (a) 2.25 kJ/mm, (b) 1.96 kJ/mm, and (c) 1.75 kJ/mm

6. CONCLUSIONS AND OUTLOOK

The following conclusions may be drawn from this analysis:

- It is possible to analyze the three-dimensional transient thermal analysis for the Keyhole PAW process using the finite element method combined with an adaptive heat source model.
- The predicted weld pool geometry and size utilizing the optimized values for certain parameters agree well with the corresponding experimentally determined values, indicating the accuracy of the approach.
- The effect of fluid flow and solidification of the weld pool are considered analytically; therefore, good predictions of the transient isotherms and the weld pool geometry are obtained.
- The results of the built model can be used for the optimization of Keyhole PAW processes to achieve sufficient energy and deep penetration.

REFERENCES

[1] Weman, K., Welding processes handbook, 1st ed., Woodhead, England, 2003, pp. 38, 39.

[2] Urena, A., Otero, E., Utrilla, M. V., and Munez, C. J., "Weldability of a 2205 duplex stainless steel using plasma arc welding," J Mater Process Technol, Vol. 182, No. 1-3, 2007, pp. 624–631.

[3] Zheng, S., Dayou, P., and Ingegerd, A., "Effect of dual torch technique on duplex stainless steel welds," Mater Sci Eng A, Vol. 356, No. 1-2, 2003, pp. 274–282.

[4] Taban, E., "Joining of duplex stainless steel by plasma arc, TIG and plasma arc+TIG welding processes," Mater Manuf Process, Vol. 23, No. 8, 2008, pp. 871–878.

[5] Taban, E., "Toughness and microstructural analysis of super duplex stainless steel joined by plasma arc welding," J Mater Sci, Vol. 43, No. 12, 2008, pp. 4309–4315.

[6] Migiakis, K., Daniolos, N., and Papadimitriou, G. D., "Plasma keyhole welding of UNS S32760 super duplex stainless steel: microstructure and mechanical properties," Mater Manuf Process, Vol. 25, No. 7, 2010, pp. 598–605.

[7] Keanini, R. G., and Rubinsky, B., "Three-dimensional simulation of the plasma arc welding process," Int J Heat Mass Transfer, Vol. 36, No. 13, 1993, pp. 3283–3298.

[8] Fan, H. G., and Kovacevic, R., "Keyhole formation and collapse in plasma arc welding," J Phys D Appl Phys, Vol. 32, No. 22, 1999, pp. 2902–2909.

[9] Wu, C. S., Wang, H. G., and Zhang, Y. M., "A new heat source model for keyhole plasma arc welding in FEM analysis of the temperature profile," Weld J, Vol 85, No. 12, 2006, pp. 284–291.

[10] Wu, C. S., Hu, Q. X., and Gao, J. Q., "An adaptive heat source model for finite-element analysis of keyhole plasma arc welding," Comput Mater Sci, Vol. 46, No. 1, 2009, pp. 167–172.

[11] Wang, H. X., Wei, Y. H., and Yang, C. L., "Numerical simulation of variable polarity vertical-up plasma arc welding process," Comput Mater Sci, Vol. 38, No. 4, 2007, pp. 571–587.

[12] ABAQUS User's Manual, Version 6.10, Karlsson & Sorensen, Inc., Hibbitt, 2010.

[13] Labudovic, M., Hu, D., and Kovacevic, R., "Three-dimensional finite element modelling of laser surface modification," I Mech E, Vol. 214, No. 8, 2000, pp. 683–692.

[14] Punitharani, K., Murugan, N., and Sivagamai, S. M., "Finite element analysis of residual stresses and distortion in hard faced gate valve," J Sci Ind Res, Vol. 69, No. 2, 2010, pp. 129–134.

[15] Jiang, W., Yahiaoui, K., Hall, F. R., and Laoui, T., "Finite element simulation of multipass welding: full three-dimensional versus generalized plane strain or axisymmetric models," J Strain Analysis, Vol. 40, No. 6, 2005, pp. 587–597.

[16] Deng, D., and Murakawa, H., "Numerical simulation of temperature field and residual stress in multi-pass welds in stainless steel pipe and comparison with experimental measurements," Comput Mater Sci, Vol. 37, 2006, pp. 269–277.

[17] Deng, D., and Murakawa, H., "Finite element analysis of temperature field, microstructure and residual stress in multi-pass buttwelded 2.25Cr–

1Mo steel pipes," Comput Mater Sci, Vol. 43, 2008, pp. 681–695.

[18] Abid, M., and Qarni, M. J., "3D thermal finite element analysis of single pass girth welded low carbon steel pipe-flange joints," Turkish J Eng Env Sci, Vol. 33, 2009, pp. 1–13.

[19] Bonifaz, E. A., and Richards, N. L., "Modeling cast IN-738 superalloy gas tungsten arc welds," Acta Materialia, Vol. 57, 2009, pp. 1785–1794.

[20] Deng, D., "FEM prediction of welding residual stress and distortion in carbon steel considering phase transformation effects," Mater and Des, Vol. 30, 2009, pp. 359–366.